# Numerical calculation of the light propagation in tapered optical fibers for optical neural interfaces

Rosa Mach-Batlle,[*,†] Marco Pisanello,[†] Filippo Pisano,[†] Massimo De Vittorio,[†,‡] Ferruccio Pisanello,[†] and Cristian Ciracì[*,†]

†*Center for Biomolecular Nanotechnologies, Istituto Italiano di Tecnologia, Via Barsanti 14, 73010 Arnesano (LE), Italy*

‡*Dipartimento di Ingegneria dell'Innovazione, Università del Salento, Lecce, Italy.*

E-mail: rosa.machbatlle@iit.it; cristian.ciraci@iit.it

**Abstract**

As implantable optical systems recently enabled new approaches to study the brain with optical radiations, tapered optical fibers emerged as promising implantable waveguides to deliver and collect light from sub-cortical structures of the mouse brain. They rely on a specific feature of multimodal fiber optics: as the waveguide narrows, the number of guided modes decreases and the radiation can gradually couple with the environment. This happens along a taper segment whose length can be tailored to match with the depth of functional structures of the mouse brain, and can extend for a few millimeters. This anatomical requirement results in optical systems with an active area very long compared to the wavelength of the light they guide and their behaviour is typically estimated by ray tracing simulations, being finite-elements methods computationally too heavy. Here we present a computational technique that exploits the beam-envelope method and the cylindrical symmetry of the fibers to provide an efficient and exact calculation of the electric field along the fibers, which may enable the design of neural interfaces optimized to meet different goals.

## Keywords

fiber optics, fiber probe, tapered fibers, computational technique, waveguide, photonics


# 1 Introduction

Optogenetics is a powerful technique that uses light to control the electrical activity of neurons genetically modified to be light sensitive.[1,2] In the last decade, this tool has been able to revolutionize the field of neuroscience because it allows for cell-type specificity, it provides very high spatial and temporal precision, and it can target multiple areas of the brain with multiple wavelengths.[3] Moreover, some of the tools used in optogenetics to deliver light to the brain, including optical fibers, have been shown to allow the recording of the optical activity of different indicators and molecules.[4,5]

The design of optical neural interfaces able to deliver light in a controlled manner in deep brain regions is an essential ingredient to achieve an optimal interaction with neurons and exploit the full potential of optogenetics.[6] While flat cleaved fiber optics enable an efficient and controllable targeting of shallow brain regions, the targeting of elongated structures (beyond 1 mm) is prohibited by tissue scattering and absorption.[7–9] A promising candidate for developing a new generation of neural interfaces able to target deep regions extending up to 3 mm are tapered optical fibers, which can perform both homogeneous light delivery and dynamically-controlled spatially-restricted illumination of the brain.[10,11] By tuning the input light distribution and the fiber numerical aperture and tapering angle one can control how the light reaches the brain. Indeed, as the waveguide narrows the number of supported modes decreases, and non-guided modes can couple energy with the environment. It has been demonstrated that the taper operates a mode-division demultiplexing of guided light, and on this bases it was possible to exploit its peculiar properties to obtain depth-resolved optical neural interfaces. The smaller the incident beam input angle with respect to the fiber axis, the deeper the region where the fiber delivers light, which offers the possibility of

targeting different brain areas along the implant axis in a reduced-invasivity fashion.[12–16]

In order to match the spatial extent of elongated brain regions and achieve an effective mode-division demultiplexing, the length of the tapered region must be of the order of some millimeters, much larger than the wavelength range typically employed in optogenetics (450 - 600 nm). This makes traditional finite-elements calculations computationally very heavy, and for this reason the power that is guided and delivered to the brain is usually estimated using ray tracing simulations.[10–13] These calculations help predict at what distance from the fiber tip the light is delivered but, since they fail to describe interference and diffraction phenomena, they do not provide an estimation of the electric and the magnetic field distribution in the targeted region. This fact limits our ability to optimize the delivery and collection of light and makes it difficult to design new optical neural interfaces with different functionalities.

One of the most recently exploited approaches to expand the functionalities of optical fibers consists of modifying the end-face or the tip of tapered optical fibers to include different types of structures that interact with the incident light in intriguing ways.[17,18] Several studies demonstrate that the use of plasmonic structures surrounding the fiber could help confine and concentrate light at the nanoscale.[19–22] Also, structures made of high-index dielectrics[23] or metals[24] have been shown to enable sub-diffraction light confinement. These studies usually assume single-mode optical fibers and therefore do not consider the mode-division demultiplexing of guided light in tapered optical fibers. If one had access to the field distributions along the taper as well as to the evanescent field around it, the design of all these structures could be optimized in order to further enhance the light-brain interaction and eventually lead to optimal depth-resolved optical neural interfaces.

In this work we propose a strategy for calculating the electric and the magnetic fields distribution in long tapered fibers (TFs) using a much more computationally cost-efficient method than the traditional full-wave finite-elements calculations. First, we exploit the cylindrical symmetry of the modes that the fiber can guide in such a way that the fields

are not calculated from a three-dimensional model but from the superposition of a finite set of two dimensional axisymmetric models. Second, we assume that the variation of the amplitude of the fields along the fiber axis, which is due to the light reflections at the fiber interfaces, are much slower than the light propagation constant. In this way, we do not need to calculate the field oscillations along the taper, which would require a fine mesh able to resolve the wavelength of the incident light, but the variations of a slowly varying envelope function, which can be evaluated using a much coarser mesh and, therefore, significantly reduced computation resources. To demonstrate the validity of the proposed methodology, we compare the obtained numerical results with experimental results. In particular, we compare the light delivery depth at different input angles for two different fibers.

## 2 Calculation of the incident field distribution

As a first step for calculating the field propagation in long TFs, one needs to obtain the field distribution at the input fiber facet, which will depend on the fiber geometry and materials, as well as on the excitation.

Consider a step-index optical fiber consisting of a cylindrical dielectric core of refractive index $n_1$ surrounded by a cylindrical cladding of refractive index $n_2$ slightly lower than $n_1$ in the presence of a light beam impinging with an angle $\theta_{\text{in}}$, as depicted in Fig. 1(a). When the incident light reaches the fiber entrance, it can excite one or multiple modes in the fiber. The number of modes that a fiber is able to guide depends on its numerical aperture (NA), given by $\text{NA} = \sqrt{n_1^2 - n_2^2}$, as well as on the ratio between the core radius, $a$, and the wavelength of the incident light $\lambda_0$: fibers with larger cores are able to guide a larger number of modes.

In the weakly guiding approximation ($n_2 \approx n_1$) the longitudinal components of the electric and the magnetic field ($E_z$ and $H_z$) are negligible. In this case, the fiber guides a set of linearly polarized modes, which are identified by the indexes $l$ and $m$ and denoted as $LP$ modes.[25,26] For each $(l, m)$ there are four degenerate modes sharing the same propagation

constant. The electric and magnetic field intensity profiles of these degenerate modes have the same radial dependence but they can point in the $x-$ or $y-$direction and vary with the angular position $\varphi$ as $\cos(l\varphi)$ or $\sin(l\varphi)$. The transverse profile of the incident light will tell what LP modes are guided. For a given light source one can obtain what is the power carried by each of the modes supported by the fiber as the overlapping integral between the input radiation and the $(l, m)$ modal function:[10]

$$P_{l,m,T} = \left| \frac{\int_0^{2\pi}\int_0^a \left(T_1 \mathbf{E}_\mathrm{s} \times \mathbf{h}^*_\mathrm{l,m}\right)\cdot\hat{\mathbf{z}} r dr d\varphi + \int_0^{2\pi}\int_a^\infty \left(T_2 \mathbf{E}_\mathrm{s} \times \mathbf{h}^*_\mathrm{l,m}\right)\cdot\hat{\mathbf{z}} r dr d\varphi}{\int_0^{2\pi}\int_0^a \left(\mathbf{e}_\mathrm{l,m} \times \mathbf{h}^*_\mathrm{l,m}\right)\cdot\hat{\mathbf{z}} r dr d\varphi + \int_0^{2\pi}\int_a^\infty \left(\mathbf{e}_\mathrm{l,m} \times \mathbf{h}^*_\mathrm{l,m}\right)\cdot\hat{\mathbf{z}} r dr d\varphi} \right|^2, \quad (1)$$

where $T_1$ and $T_2$ are the transmission Fresnel coefficients, $\mathbf{E}_\mathrm{s}$ is the transverse component of the electric field incident on the fiber input facet, and $\mathbf{e}_\mathrm{l,m}$ and $\mathbf{h}^*_\mathrm{l,m}$ are the transverse electric and magnetic field profiles, respectively, of a given degenerated $(l, m)$ mode. The field profiles of the LP modes are well known and they can be found in,[26] for example. The superposition of all the modes will result in the field distribution at the fiber input facet.

In our calculations we consider as a light source a linearly polarized Gaussian beam forming an angle $\theta_\mathrm{in}$ with the fiber axis. The numerical aperture of the fiber limits the input angles that can be used to couple light into the fiber to $\theta_\mathrm{a} = \sin^{-1}$ NA.[25] For a fiber with NA $= 0.22$, for example, $\theta_\mathrm{a}$ is found to be $12.7°$ and for this reason experimental data is only reported for $\theta_\mathrm{in}$ values lower than this.[11] In this range of $\theta_\mathrm{in}$, the transverse component of the electric field incident in the fiber input facet can be written as:

$$\mathbf{E}_\mathrm{s} = E_0 e^{-r^2/(2\rho_s^2)} e^{-ik_0 r \sin\theta \cos\varphi} \hat{\mathbf{y}}, \quad (2)$$

where $k_0$ is the wave number in free space, $\rho_s$ is the gaussian beam waist radius and $E_0$ is a normalization factor $E_0 = \sqrt{2\eta_0/(\pi\rho_s^2)}$. $\eta_0 = \sqrt{\mu_0/\varepsilon_0}$ is the impedance of free space, with $\mu_0$ and $\varepsilon_0$ being the vacuum permeability and permittivity, respectively. Throughout this work

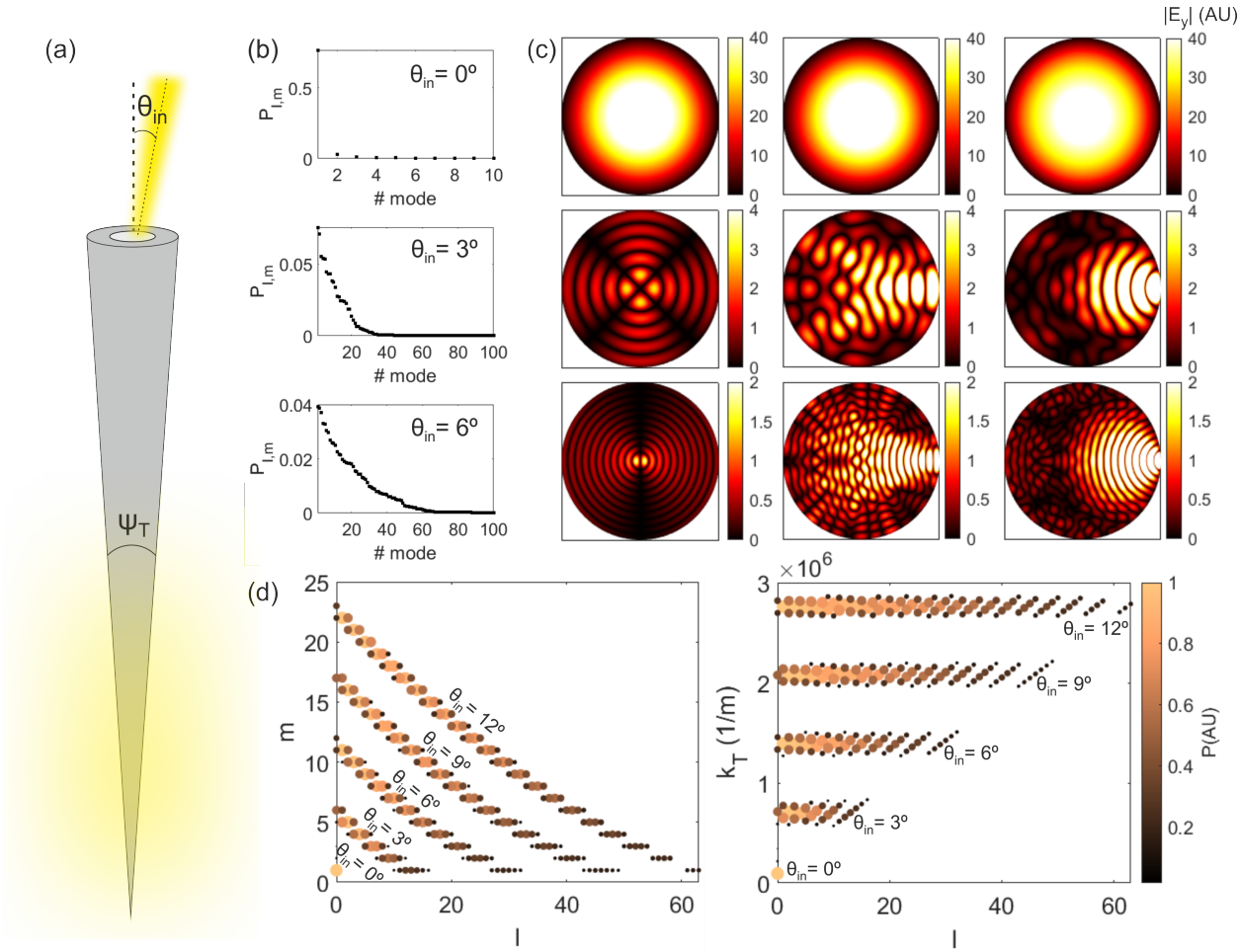


Figure 1: (a) Sketch of a step-index tapered optical fiber. (b) Power guided by the modes supported by a $NA = 0.22$ fiber of core diameter $a = 50$ nm when excited by a $y-$polarized Gaussian beam of wavelength $\lambda_0 = 473$ nm, waist radius $\rho_s = 25/\sqrt{2}$ and incident angle $\theta_{\rm in} = 0°$, $\theta_{\rm in} = 3°$, and $\theta_{\rm in} = 6°$. The modes are ordered according to the power they guide, so for each $\theta_{\rm in}$ the mode number 1 is the one guiding the largest power. (c) Absolute value of the component $E_y$ of the electric field at the input core facet of the TF in (b) for $\theta_{\rm in} = 0°$ (top), $\theta_{\rm in} = 3°$ (middle), and $\theta_{\rm in} = 6°$ (bottom) considering the mode guiding the largest power (left) and the superposition of the modes guiding at least a 50% (middle) and a 95% (right) of the total guided power. (d) Numbers $l$ and $m$ and transverse component of the propagation constant $k_{\rm T}$ of the modes guiding the 95% of the total power guided by the fiber for $\theta_{\rm in}$: $0^{\rm o}$, $3^{\rm o}$, $6^{\rm o}$, $9^{\rm o}$, and $12^{\rm o}$. The color and size of the markers indicate the power of each mode normalized to the power of the mode guiding the largest power for each $\theta_{\rm in}$.

we consider that the incident light wavelength is $\lambda_0 = 473$ nm because this is the wavelength at which one of the most common proteins involved in optogenetics, Channelrhodopsin-2 (ChR2), is maximally activated but all the parameters we use in the simulations can be tuned to meet the requirements of different optogenetics tools.[27]

Figure 1(b) shows the power guided by the modes supported by a fiber with NA = 0.22 and core diameter $a = 100$ nm for three different incident angles of a linearly polarized Gaussian beam of waist radius $\rho_s = 25/\sqrt{2}$ $\mu$m calculated using Eqs. (1) and (2). The modes are sorted in such a way that mode 1 is the one guiding the largest power and the power decreases as the mode number increases. It can be seen that the larger the incident angle is, the larger the number of modes that guide an appreciable proportion of the incident light power.

The electric field distribution at the input fiber facet can be obtained as the sum of the electric field created by all the modes supported by the fiber, each of them weighted according to the power they guide for each incident angle. Figure 1(c) illustrates the field distribution at the core input facet of the fiber calculated taking into account only the mode guiding the highest power (left) and the superposition of all the modes guiding a 50% (middle) and a 95% (right) of the total guided power for the three incident angles in Fig. 1(b). These examples demonstrate that for incident angles different from 0° the field distribution will strongly depend on the number of modes taken into account in the calculations.

Finally, Fig. 1(d) illustrates that the larger the input angle, the wider the range of mode numbers $l$ and $m$ that are excited with a significant portion of the power (left) and the larger the transverse component of the propagation constant $k_{\mathrm{T}}$ associated to the guided modes (right). For each incident angle, the larger the mode number $l$, the lower the mode number $m$ of the guided modes and the lower the portion of the power that is guided.

# 3 Beam envelope method for calculating the field propagation in long optical fibers

Computing the field at the fiber input is the first step toward obtaining the electric and the magnetic field distribution that reaches the outer surface of the TF and, therefore, is delivered to a targeted region of the brain. To this end, one could think of creating a three-dimensional (3D) model of the long TF with the calculated input field distribution at the fiber entrance. However, this model would require an extremely thin mesh compared to the dimensions of the fiber, resulting in very high computational demands. Indeed, standard taper lengths are >1 mm, which is more than three orders of magnitude longer than the standard wavelength $\lambda_0 = 473$ nm. Since one usually needs at least 5 nodes per wavelength (in the medium) to resolve a wave oscillation, the calculations would require a very fine mesh in the axial fiber direction [hereafter referred to as $z-$, see axes definition in Fig. 2(a)]. Moreover, one would also need to discretize a large 3D space with a mesh sufficiently thin in the $x$- and $y$-directions to resolve all the light reflections along the taper interfaces. Thus, some strategies for reducing the computation requirements are necessary.

To this aim, the 3D problem can be converted into a set of two-dimensional (2D) axisymmetric problems. Even though the field distribution at the fiber entrance is not axisymmetric [Fig. 1(c)], it can be written as the superposition of a set of cylindrical harmonics whose azimuthal dependence is of the form $e^{im_{\mathrm{az}}\varphi}$, with $m_{\mathrm{az}}$ being an integer. Because the geometry is axisymmetric, each cylindrical harmonic propagates independently. The full 3D problem then can be reduced to a set of 2D problems corresponding to different values of $m_{\mathrm{az}}$.[28,29]

In order to perform the axisymmetric calculations, the field distribution of each mode must be written in cylindrical coordinates. Assuming that the incident field was polarized in the $y$-direction, the angular and the radial components of the electric field distribution of

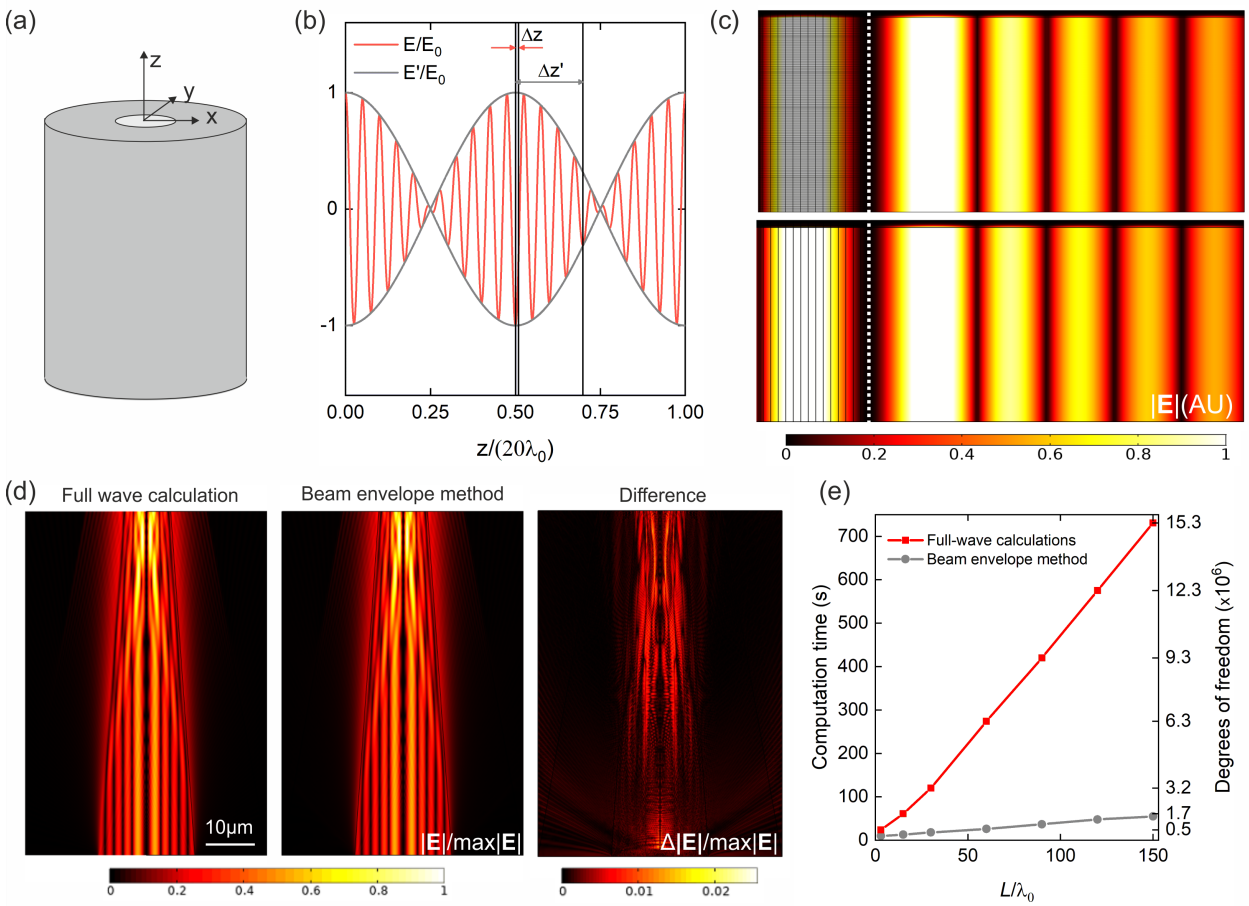


Figure 2: (a) Sketch of a segment of length $L$ of a step-index optical fiber. (b) Example of the propagation of the electric field **E** and its envelope **E'** normalized to the incident field amplitude $E_0$ illustrating the required minimum mesh elements size to resolve both waves (5 nodes per wavelength). (c) Electric field in the core of a segment of length $L = 30\lambda_0/n_1$ of a step-index optical fiber of $NA = 0.22$ and core diameter $a = 50$ nm when excited with the mode $l = 2$, and $m = 5$. The first panel corresponds to the calculation with traditional finite elements and the second panel to the calculation with the beam envelope method. For comparison, the mesh used in these calculations is shown in the left side of the plots. The dotted white line indicates the fiber axis. (d) Propagation of the mode mode $l = 2$ and $m = 5$ along a fraction of length $L = 150\lambda_0$ of a TF of $NA = 0.22$ and tapering angle $\psi_{\mathrm{T}} = 20°$ obtained from a full wave calculation (left panel), using the beam envelope method (central panel), and the difference between them (right panel). (e) Comparison between the computation time and the degrees of freedom required to calculate the electric field propagation in different fractions of the TF shown in (d) for the traditional full-wave finite elements and the beam envelope method calculations.

the mode $(l, m)$ can be written as:

$$E_\varphi = R_{\mathrm{l,m}}(r)\cos(l\varphi)\cos(\varphi) = \frac{1}{4}R_{\mathrm{l,m}}(r)\left(\mathrm{e}^{i(l+1)\varphi} + \mathrm{e}^{-i(l+1)\varphi} + \mathrm{e}^{i(l-1)\varphi} + \mathrm{e}^{-i(l-1)\varphi}\right), \quad (3)$$

$$E_\rho = R_{\mathrm{l,m}}(r)\cos(l\varphi)\sin(\varphi) = \frac{i}{4}R_{\mathrm{l,m}}(r)\left(-\mathrm{e}^{i(l+1)\varphi} + \mathrm{e}^{-i(l+1)\varphi} + \mathrm{e}^{i(l-1)\varphi} - \mathrm{e}^{-i(l-1)\varphi}\right), \qquad (4)$$

where $R_{\mathrm{l,m}}(r)$ and $\cos(l\varphi)$ are the radial and the angular dependence of the $y$ component of the $(l, m)$-mode electric field.[25] These equations show that the propagation of each mode can be obtained as a result of two axisymmetric calculations, with azimuthal mode numbers $m_{\mathrm{az}} = (l \pm 1)$; calculations with $\pm m_{\mathrm{az}}$ azimuthal mode numbers give symmetric results and therefore the number of calculations required can be halved.

Next, we will explore if the computational cost of the simulations can be further reduced using the beam-envelope method. Imagine an electromagnetic wave with electric field $\mathbf{E}$ propagating along the $z-$direction with propagation constant $\beta$. In this case, the electric field can be written as $\mathbf{E}'\mathrm{e}^{-i\beta z}$, where $\mathbf{E}'$ has a constant amplitude along $z$. Let us assume that the wave encounters a material boundary that is slightly tilted with respect the propagation direction and, therefore, it is partially reflected. One is still be able to write the electric field as $\mathbf{E}'\mathrm{e}^{-i\beta z}$, but due to the reflections at the fiber boundaries, the amplitude of $\mathbf{E}'$ is not constant but corresponds to a varying envelope function, as illustrated in the example in Fig. 2(b). In cases where the field propagation constant $\beta$ is known and the envelope varies slowly, one can apply the beam-envelope method to calculate the field distribution by solving the wave equation not for $\mathbf{E}$ but for $\mathbf{E}'$. Since $\mathbf{E}'$ may vary much slowly in the $z-$direction than $\mathbf{E}$ it can be resolved by a much coarser mesh and, as a result, it may require a much lower computational time [mesh size illustrated in Fig. 2(b)]. In order to solve for the slowly varying envelope function, one needs to substitute $\mathbf{E}$ by $\mathbf{E}'\mathrm{e}^{-i\beta z}$ in the wave equation, $\nabla \times (\mu_r^{-1}(\nabla \times \mathbf{E})) - \epsilon_r k_0^2 \mathbf{E} = 0$, which gives

$$\nabla \times \left(\mu_r^{-1}(\nabla \times \mathbf{E}')\right) - \epsilon_r k_0^2 \mathbf{E}' - \beta\left(\beta \mathbf{E}' + 2i\frac{\partial \mathbf{E}'}{\partial z}\right) = 0. \qquad (5)$$

In our study it is possible to implement this method because we calculate the propagation of each guided mode independently and for each mode $(l, m)$ the initial propagation constant $\beta_{l,m}$ is well known. We have manually implemented this method in the Radio Frequency:

Electromagnetic Waves module of Comsol Multiphyics as described in the Methods section. Similar envelope models have been applied in laser plasma accelerators, in which laser pulses are guided along very long channels compared to the laser wavelength.[30–32] It differs from the beam propagation method[33,34] and the parabolic equation method,[35] both used to simplify the calculations in long waveguides, because it retains the second order derivatives and hence does not give an approximation but the exact solution of the field distribution, provided that the envelope oscillations are well resolved.

To verify that the envelope method is well implemented, we compare the field distribution obtained using this strategy to the result obtained with traditional finite-elements calculations. First, we consider a short segment of length $L$ of a flat step-index weakly guiding optical fiber of core and cladding refractive indexes, $n_1 = 1.464$ and $n_2 = 1.447$, and core and cladding diameters $a = 50$ $\mu$m and $b = 125$ $\mu$m, respectively. As a light source, we consider a linearly polarized Gaussian beam forming an angle $\theta_{\text{in}} = 3°$ with the fiber axis. We calculate the propagation of the mode $l = 2, m = 5$, which guides the largest portion of the total power guided for this incident angle. The field distribution of this mode at the fiber entrance was shown in Fig. 1(c). As shown in Fig. 2(c) both methods give the same field distribution along the whole length of the fiber. The meshes are compared on the left side of Fig. 2(d). In both cases we have considered the same number of points in the radial direction and the minimum number of mesh elements required for calculating the mode propagation. In the case of the traditional finite-elements calculations, each wavelength is resolved by 5 points (in the $z-$direction). In contrast, the beam-envelope method makes it possible to calculate the envelope propagation using a single element for all the length [Fig. 2(c) bottom] and, therefore, the mesh elements do not vary with $L$. Thus, while the computation time required to perform a traditional finite elements calculation linearly increases with the fiber length, the computation time of the beam-envelope calculations does not depend on the fiber length, it remains constant at 3 s.

This case corresponds to an ideal scenario in which there are no light reflections and

the amplitude of the envelope is constant, i.e. it does not oscillate with $z$, and one is able to carry out the envelope-function calculations using a single mesh element. In general, including the cases we will study below, there are reflections in the fiber due to the tapering, for example, which results in oscillations in the electric field envelope and a mesh that resolves the envelope oscillations is needed. In order to verify that our method gives accurate results also when there are reflections in the fiber, we assume that the fiber considered in Fig.2(c) is tapered, with a tapering angle $\psi_{\mathrm{T}} = 20°$. The field is calculated on a short fraction of the fiber so the traditional finite-elements calculations can run in some minutes. Results in Fig. 2(d) illustrate that the field distribution of the mode $l = 2$, $m = 5$ in a fraction of a TF with input facet core radius $a = 10$ $\mu$m and length $L = 150$ $\lambda_0$ obtained with the beam-envelope method looks identical to the field distribution obtained with traditional full-wave calculations: the difference between both calculations is smaller than 2.5%. Finally, Fig. 2(e) shows the computational time required to calculate the field distribution along different portions of the fiber in (d) with both methods. The computational time increases with the fiber length, but it is much lower when using the envelope function than when using the traditional finite-elements calculations, specially when considering long fibers.

# 4 Results and discussion

We can now apply the proposed strategy to calculate the field distribution in long tapered optical fibers. Since we are interested in comparing our results with experimental data, we focus on the analysis of two different fibers whose behaviour as neural interfaces has already been experimentally characterized.[11,13]

The first fiber is defined by the following parameters: numerical aperture NA= 0.22, core and cladding diameters $a = 50$ $\mu$m and $b = 125$ $\mu$m, respectively, and core and cladding refractive indexes $n_1 = 1.464$ and $n_2 = 1.447$, respectively. The second fiber is defined by NA= 0.66, $a = 200$ $\mu$m, $b = 230$ $\mu$m, $n_1 = 1.63$, and $n_2 = 1.49$. The fibers are assumed

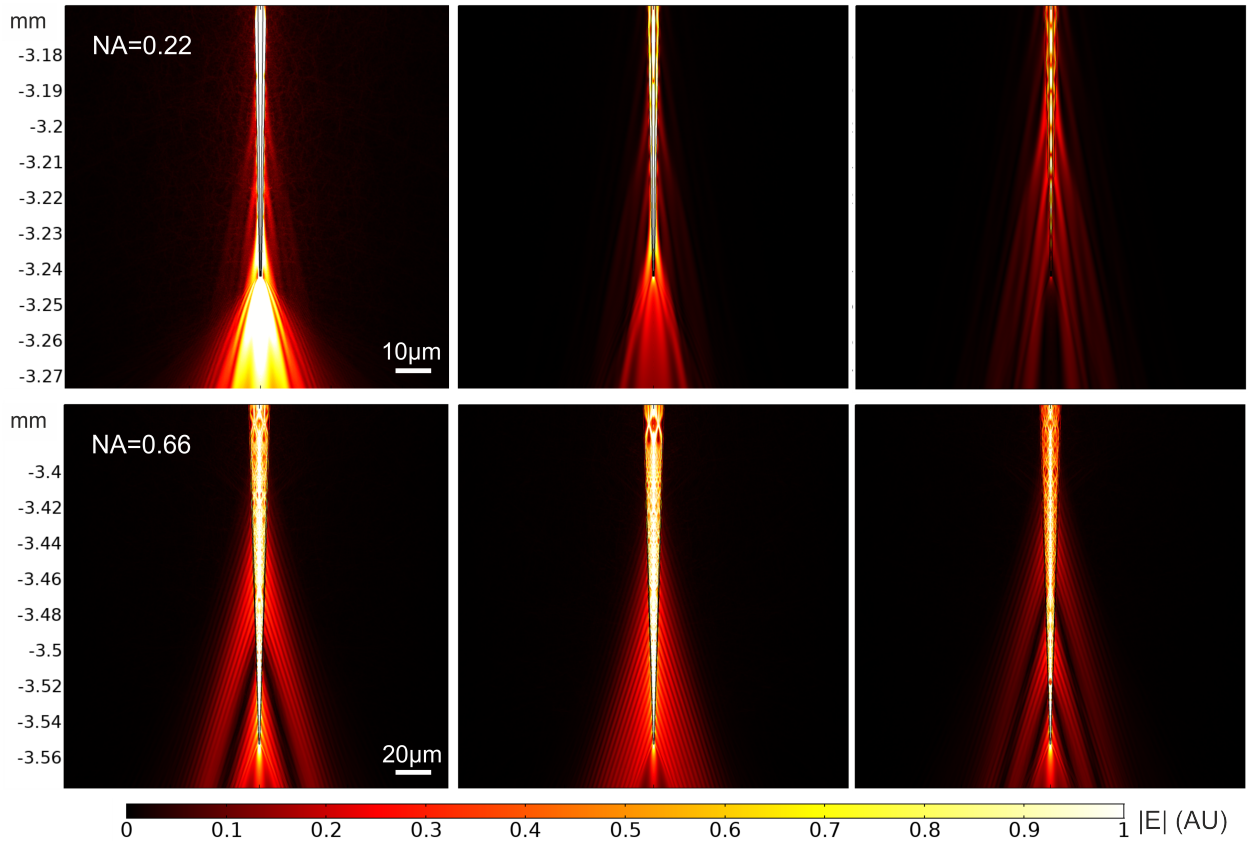


Figure 3: Propagation of the three modes guiding the largest power when the NA = 0.22 (top) and the NA = 0.66 (bottom) fibers are excited with an incident angle $\theta_{\rm in} = 0°$.

to be surrounded by water, with refractive index $n_w = 1.33$. The tapering angle [defined in Fig.1(a)] is $\psi_{\rm T} = 2.2°$ for the NA= 0.22 fiber and $\psi_{\rm T} = 3.7°$ for the NA= 0.66 fiber. The fiber tip is assumed to be cut at a diameter $d_{\rm T} = 500$ nm, which leads to a fiber length, $L_{\rm T}$, of 3.242 mm and 3.553 mm for the NA= 0.22 and the NA= 0.66 fibers, respectively. In all the calculations we will consider a linearly $y-$polarized Gaussian beam of wavelength $\lambda_0 = 473$ nm forming an angle $\theta_{\rm in}$ with the fiber axis. For fibers with NA= 0.22 the maximum $\theta_{\rm in}$ that will be considered is $\theta_{\rm in} = 12°$, while for NA= 0.66 fibers the incident angle can go up to $\theta_{\rm in} = 33°$ due to their larger numerical aperture.

To start with, consider an incident angle $\theta_{\rm in} = 0°$. It can be obtained from Eqs. (1) and (2) that for this incident angle the 95% of the total power guided by the fiber is guided by only three modes, both for NA= 0.22 and NA= 0.66 fibers. The modulus of the electric field

distribution in the tip of these fibers is shown in Fig. 3 for these three modes. We only plot here the field at the very tip of the fiber for illustration purposes (the fiber entrance is set at $z = 0$ mm), as in this way it is possible to observe how the field of each mode is delivered to the fiber surrounding media.

The number of modes that guide a significant fraction of the power increases with the incident angle, as seen above [Fig. 1(b)], which makes it difficult to illustrate the propagation of all the excited modes for the other $\theta_{\text{in}}$. However, one can still compare the field propagation of the mode guiding the largest fraction of the power for different $\theta_{\text{in}}$. The propagation of these modes are shown in Fig. 4, using intervals of 2° for the NA= 0.22 fiber and 5° for the NA= 0.66 fiber. Figure 4 shows that for both numerical apertures low input angles generate the light delivery close to the tip, while increasing $\theta_{\text{in}}$ moves the emission farther from it. This result is in agreement with the theoretical and the experimental results reported in the literature.[10,11,13]

The light delivery to the surrounding media can be further characterized by analysing how the delivery distance from the tip depends on the light incident angle. Figure 5(a) shows the profile of the square of the electric field, which is proportional to the light intensity, along a line parallel to the external surface of the TF for all the modes in Fig. 4. The field is measured in the surrounding media, at 0.5 $\mu$m from the fiber surface (moving in the radial direction). From these intensity profiles one can calculate the starting emission diameter, which is found as the fiber diameter at which the modulus of the intensity is a 90% of half its peak value, and the centroid distance from the tip, defined as the distance at which the integral of the intensity from the tip to that point corresponds to more than 50% of the same integral along the whole taper surface, from the tip to the input facet of the fiber. Both the starting emission diameter and the centroid distance from the tip are found to increase linearly with the incident angle [Fig. 5(b)]. This is because the transverse component of the propagation constant of the guided modes, $k_{\text{T}}$, which defines the fiber diameter where the modes become evanescent and, thus, are not guided anymore, increases linearly with $\theta_{\text{in}}$

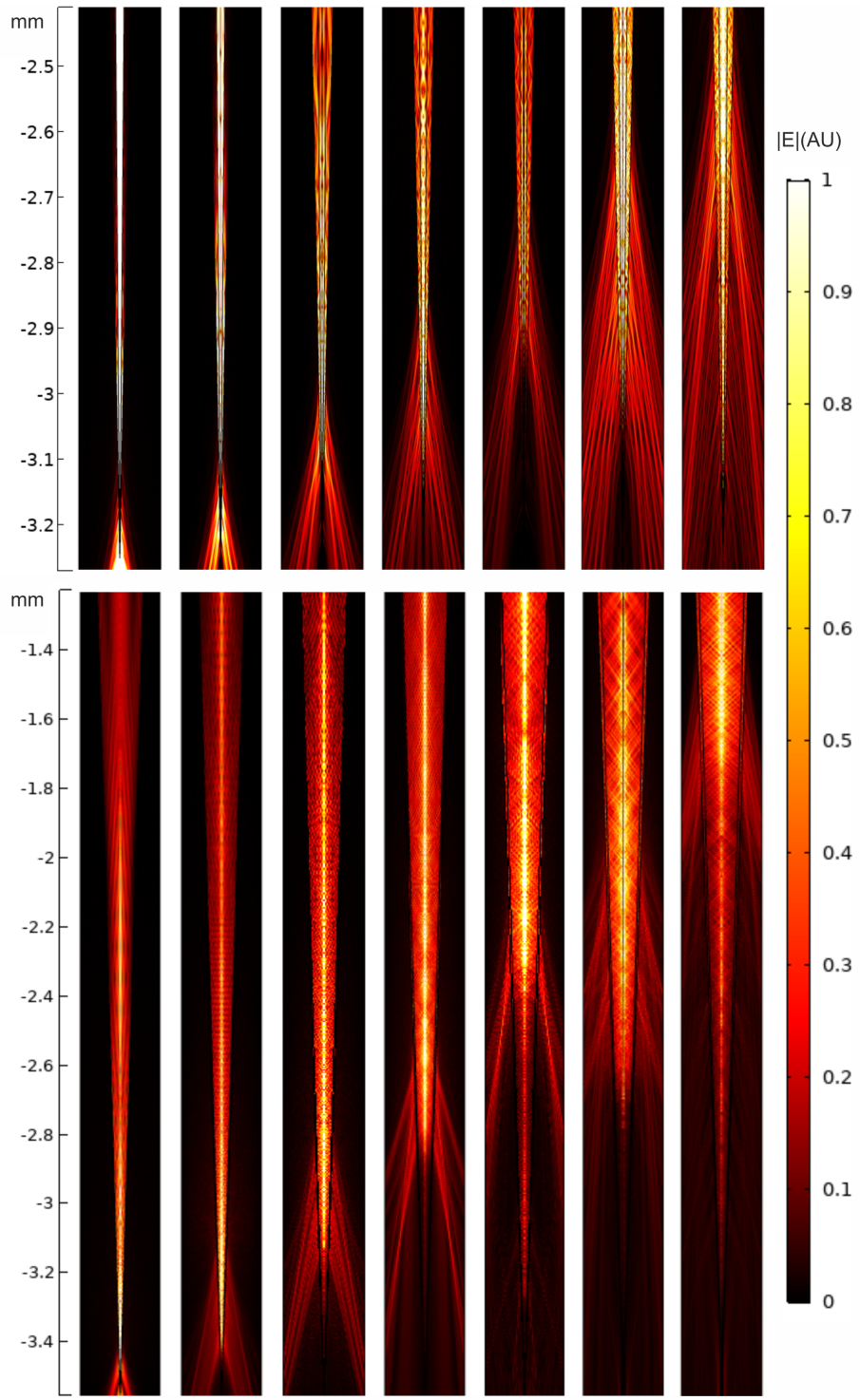


Figure 4: Propagation of the mode guiding the largest power when the NA = 0.22 (top panels) and the NA = 0.66 (bottom panels) fibers are excited with incident angles (from left to right) $\theta_{\text{in}} = 0°$, 2°, 4°, 6°, 8°, 10°, and 12°, and $\theta_{\text{in}} = 0°$, 5°, 10°, 15°, 20°, 25°, and 30°, respectively.

[Fig. 5(c)].

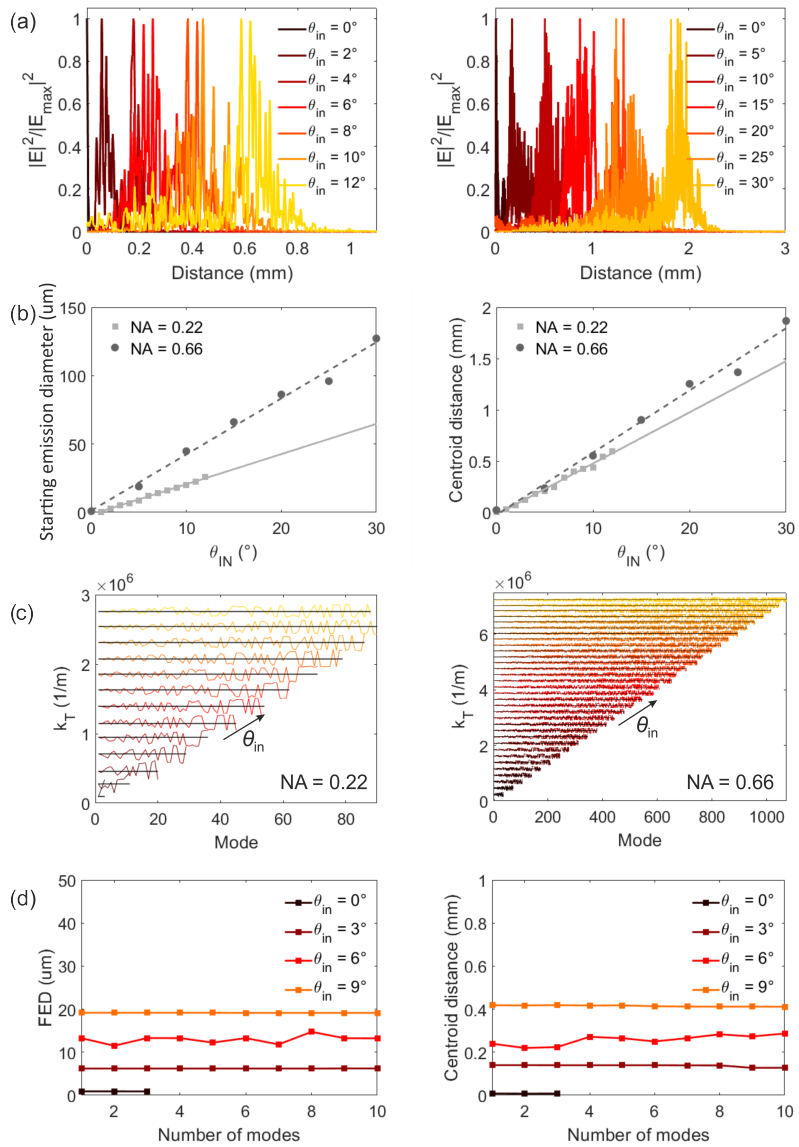


Figure 5: (a) Square of the modulus of the electric field $|E|^2$ at 0.5 $\mu$m from the fiber surface as a function of the distance from the tip for different incident angles for the NA= 0.22 fiber (left) and the NA= 0.66 fiber (right). For each incident angle, results correspond to the mode guiding the largest fraction of the total guided power and are normalized to the maximum square of the modulus of the electric field, $|E_{\max}|^2$, for that angle. (b) Starting emission diameter and centroid distance from the tip as a function of the incident angle. The points correspond to the results obtained from the lines in (a) and the lines give the linear fitting of the data. (c) Transverse component of the propagation constant of the modes guiding a 95% of the total guided power sorted in such a way that mode 1 corresponds to the mode guiding the largest fraction of the power for each $\theta_{\text{in}}$. Each color corresponds to a different input angle. (d) Starting emission diameter and centroid distance from the tip for different incident angles as a function of the number of modes that are computed.

In order to compare these results to the experimental data reported in previous works,[11,13] we first need to verify that the starting emission diameter and the centroid distance calculated assuming just one mode for each $\theta_{\rm in}$ are a good approximation to the results we would obtain if all the modes that are excited for each $\theta_{\rm in}$ were taken into account. To this end, we calculate the starting emission diameter and the centroid distance from the tip assuming the superposition of different number of modes for different incident angles, from a single mode to ten modes. Since the field distribution corresponding to the superposition of modes is not axisymmetric [see Fig. 1(c)], the field profiles have been obtained by averaging the field distribution along $\varphi$ (at 0.5 $\mu$m from the fiber surface, as above). As shown in Fig. 5(d) the results for the different number of modes are approximately the same for all the considered input angles: a single mode seems to be enough to estimate the starting emission diameter and the centroid distance from the tip. This can be understood from the plots in Fig. 5(c). Since all the modes that are excited for a given $\theta_{\rm in}$ have a very similar propagation constant, which oscillates around the propagation constant of the mode guided with the largest power for each $\theta_{\rm in}$, they all become evanescent at a similar distance from the fiber tip. Therefore, the starting emission diameter and the distance from the tip must be approximately the same for all the modes excited with the same $\theta_{\rm in}$. This is illustrated in the example in Fig. 3, as the starting emission diameter of the three modes that are guided for each fiber (all three excited with $\theta_{\rm in} = 0°$) is approximately the same.

Finally, we can compare the centroid distance from the tip obtained with the numerical calculations to the values obtained from the data reported in Refs. 11 and 13 for the TFs with NA = 0.22 and NA = 0.66, respectively. Experimental light emission profiles were measured from the fluorescence intensity generated by a TF immersed in an homogeneous bath (PBS:Fluorescein 30 $\mu$M). Using a fast laser scanning system, the laser input angle $\theta_{\rm in}$ was controlled to launch modes with a defined transverse component $k_{\rm T}$ in a patch cord butt-coupled to the TF in exam. Briefly, a CW laser beam (473 nm, Ciel, Laser Quantum) was focused on a galvanometric mirror that deflects the incoming light at an angle proportional

to its driving voltage. The laser beam deflected by the mirror is collected and collimated by a first aspheric lens (focal length 100 mm) and focused on the patch cord input core with a second aspheric lens (focal length 32 mm). The fluorescent light generated by the fiber emission is imaged on a sCMOS camera, synchronized with the scanning mirror, that produces images with a discretization of 0.522 px/$\mu$m. This system allows us to image the light emission profiles generated by input angles covering the full angular acceptance of the two fibers, with steps of 0.5°.

For a better comparison with the experimental data, instead of considering a single field profile as in Fig. 5(a), we average the electric field along a set of 21 parallel lines. The first line is set at the fiber surface and the last one at a distance of 2 $\mu$m from the surface, so the spacing between lines is 0.1 $\mu$m. For each incident angle, we obtain the centroid of the emission region as $\mu = \int_{z=0}^{z=L} I(z) z \mathrm{d}z / \int_{z=0}^{z=L} I(z) \mathrm{d}z$, where $L$ is the length of the fiber,[13] and the standard deviation of the data as $\sqrt{\int_{z=0}^{z=L} I'(z)(z-\mu)^2 \mathrm{d}z}$, where $I'(z)$ is $I(z)/\int_{z=0}^{z=L} I(z)\mathrm{d}z$. Results are shown in Fig. 6. For the experimental data we have calculated the centroid distance from the tip taking into account the data above the peak half prominence;[13] this avoids the influence of fluorescence tails excited in the medium by the light emitted from the active region. Notice that, since we do not consider data beyond the tip, the centroid we obtain does not always correspond to the point where the field is maximum. This is evident in Fig. 6(a) for the NA= 0.22 fiber with an input angle of 0º: the centroid distance from the tip obtained from the experimental data (the profiles are shown in the inset) is found to be 0.13 mm, but looking at the profile in the inset one sees that the maximum of the intensity is at 0 mm.

Figure 6 shows that the numerical results exhibit a similar trend to that of the experimental results: the centroid distance from the tip increases approximately linearly with the incident angle with a relatively good agreement. For low input angles, and in particular for $\theta_{\mathrm{in}} = 0°$, the theoretical centroid is close to the fiber tip and has a lower standard deviation, which differs from the experimental results, which exhibit an approximately constant

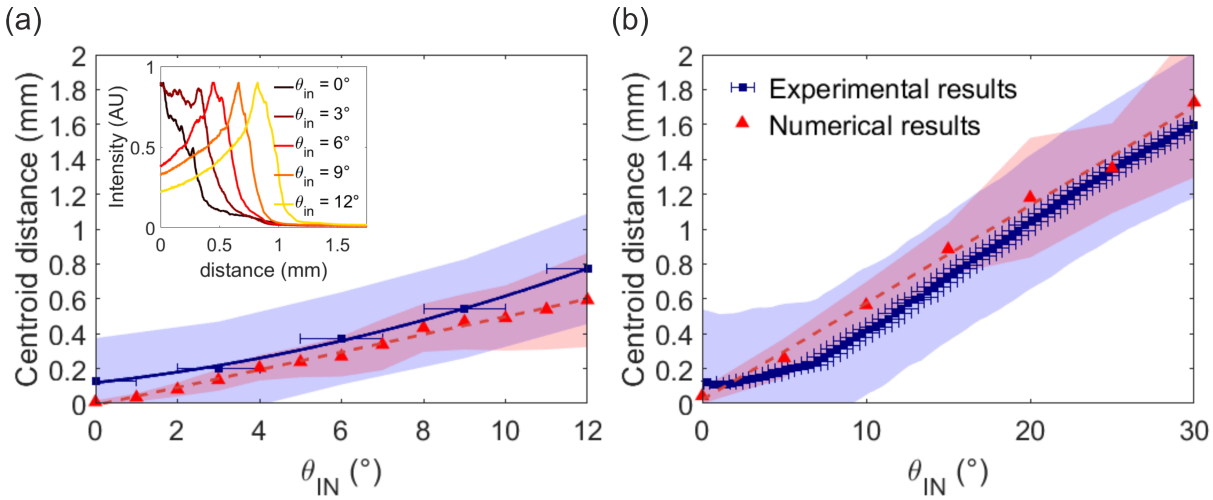


Figure 6: Centroid distance from the tip for the (a) NA= 0.22 and (b) NA= 0.66 tapered fibers calculated from the intensity profiles obtained from the experimental data (blue squares) and from the numerical calculations (red triangles). The solid and dashed lines are guides for the eye. The experimental results have a convergent input beam of $\pm 1°$, used to report the horizontal error bars. The blue and the red shadowed regions are bounded by the centroid distance from the tip $\pm$ the standard deviation, which gives an idea of the emission region. The inset in (a) shows the experimental intensity profile along the surface of the NA=0.22 fiber for each incident angle.

standard deviation for all the input angles. For example, for NA=0.22 and $\theta_{\text{in}} = 0°$ the numerical results indicate that the centroid of the emission occurs at the taper's tip with a standard deviation approximately zero, while the experimental results give a centroid distance from the tip of approximately 0.13 mm and a standard deviation of approximately 0.25 mm. However, both the numerical and the experimental intensity profiles for $\theta_{\text{in}} = 0°$ exhibit the maximum intensity at a distance of 0 mm from the tip [see Figs. 5(a) and 6(a), respectively]. Moreover, while the centroid distance obtained numerically increases linearly with the incident angle for the entier set of $\theta_{\text{in}}$, the numerical results deviate from a linear dependence at low input angles

At normal incidence, it can be analytically obtained that the mode guided with the largest fraction of the power ($l = 0$, $m = 1$) must reach the end of the fiber, as observed with the numerical calculations, because it becomes evanescent at a very small taper diameters (at 0.03 mm and 0.001 mm from the tip for the NA=0.22 and the NA = 0.66 fibers, respec-

tively). This difference with respect to the experimental data, in which the emission region is more broadly spread along the taper[inset in Fig. 6(a)], can be explained considering that experiments are performed by launching light in a 1m-long patch cord, whose bends and length generate modal mixing. Energy from low order modes, and in particular from mode $l = 0$, $m = 1$, can be transferred toward modes with a marginally higher $k_{\mathrm{T}}$,[36,37] generating a longer emission region in the experiments for low $\theta_{\mathrm{in}}$.

Additionally, in the calculations we have assumed a perfectly linear taper profile and that both the core and the cladding of the fiber linearly decrease as one approaches the fiber tip in such a way that the ratio between the cladding and the core diameters is kept constant, but we cannot confirm that this is the case for the actual fiber. Similarly, the core and cladding of the actual fiber which start being concentric at the input facet could lose the symmetry as the fiber becomes thinner. Finally, all the assumed parameters (the refractive indexes and core and cladding diameters) were assumed as the nominal manufactures' value, and the datasheet tolerances were not considered.

In conclusion, in this work we have presented a strategy to significantly reduce the computation cost and time required to calculate the wave propagation in long tapered optical fibers. We have applied this method to obtain the field distribution along tapered optical fibers of numerical aperture NA= 0.22 and NA= 0.66 assuming an incident Gaussian beam forming different angles with the fiber axis. Results have shown that the starting emission diameter and the intensity centroid distance from the tip of the fiber linearly increase with the light incident angle. We have also demonstrated that the calculation of a single mode is enough to estimate the starting emission diameter and the centroid distance from the tip, characterizing in this way the light delivery region as a function of the incident angle. Finally, we have validated the proposed strategy by comparing the obtained numerical and experimental results. Compared to the ray tracing calculations usually employed for the theoretical characterization of tapered optical fibers, our technique gives access to the three components of the electric field along the fibers, which we believe can be exploited for

designing novel generations of neural interfaces.

# Methods

The beam-envelope method is implemented in Comsol Multiphyics by modifying the Wave equation found in the Electromagnetic Waves, Frequency domain module,

$$\int \mu_r^{-1}(\nabla \times \mathbf{E}) \cdot (\nabla \times \tilde{\mathbf{E}}). \tag{6}$$

If we substitute the electric field $\mathbf{E}$ in Eq. (6) by $\mathbf{E}'\mathrm{e}^{-i\beta_{l,m}z}$, where $\mathbf{E}'$ is the electric field of the slowly varying envelope function and $\beta_{l,m}$ is the propagation constant of the mode $(l, m)$ in the $z-$direction, the term $(\nabla \times \mathbf{E})$ becomes

$$\nabla \times (\mathbf{E}'\mathrm{e}^{-i\beta_{l,m}z}) = (\nabla \times \mathbf{E}' - i\beta_{l,m}\mathbf{z} \times \mathbf{E}')\mathrm{e}^{-i\beta_{l,m}z} = (\nabla - i\beta_{l,m}\mathbf{z}) \times \mathbf{E}'\mathrm{e}^{-i\beta_{l,m}z}. \tag{7}$$

We modify the wave equation according to Eq. (7) - that is, we include the terms $-i\beta_{l,m}E_\rho$ and $i\beta E_\varphi$ to the expressions of the $\varphi-$component and the $\rho-$component of the curl operator, respectively. In this way, we solve the fields for the slowly varying envelope. After carrying out the calculations, we just need to multiply or results by $\mathrm{e}^{-i\beta z}$ in order to take into account the field oscillations due to the propagation constant $\beta$. Further, we assume that $\mathbf{E}'$ can be written in cylindrical coordinates as $\mathbf{E}' = \sum_n \tilde{\mathbf{E}}^{(n)}(\rho, z)e^{in\varphi}$, such that the curl operator in Eq. (7) becomes for each $n$:

$$\begin{aligned}(\nabla - i\beta_{l,m}\mathbf{z}) \times (\tilde{\mathbf{E}}^{(n)}e^{in\varphi}\mathrm{e}^{-i\beta z}) = \Bigg[\hat{\rho}\left(-\frac{\partial \tilde{E}_\varphi^{(n)}}{\partial z} - i\frac{n}{\rho}\tilde{E}_z^{(n)}\right) + \hat{\varphi}\left(\frac{\partial \tilde{E}_\rho^{(n)}}{\partial z} - \frac{\partial \tilde{E}_z^{(n)}}{\partial \rho}\right) + \\ \hat{z}\left(\frac{\tilde{E}_\varphi^{(n)}}{\rho} + \frac{\partial \tilde{E}_\varphi^{(n)}}{\partial \rho} + i\frac{n}{\rho}\tilde{E}_\rho^{(n)}\right) - i\beta_{l,m}\mathbf{z} \times \tilde{\mathbf{E}}^{(n)}\Bigg] e^{in\varphi}\mathrm{e}^{-i\beta_{l,m}z}.\end{aligned} \tag{8}$$

Note that this method is implemented in the Optics module of Comsol Multiphysics only for trivial case when $n = 0$ (axisymmetric). Since we need to perform calculations with different

values of $m_{\mathrm{az}}$, the manual implementation of the method was required.

## Acknowledgement

R.M-B., M.D.V., F. Pisanello and C.C. acknowledge funding from the European Union's Horizon 2020 research and innovation program under grant agreement No 828972. F. Pisano and F. Pisanello acknowledges funding from the European Research Council under the European Union's Horizon 2020 research and innovation program (grant agreement No 677683). M.D.V. acknowledges funding from the European Research Council under the European Union's Horizon 2020 research and innovation program (No 692943). M.D.V. is funded by the US National Institutes of Health (U01NS094190). F. Pisanello and M.D.V. are funded by the US National Institutes of Health (1UF1NS108177-01).

## Notes

Disclosures: M.D.V. and F. Pisanello are founders and hold private equity in Optogenix, a company that develops, produces and sells technologies to deliver light into the brain. Tapered fibers commercially available from Optogenix were used as tools in the research.

## References

(1) Miesenböck, G. The optogenetic catechism. *Science* **2009**, *326*, 395–399.

(2) Deisseroth, K. Optogenetics: 10 years of microbial opsins in neuroscience. *Nature Neuroscience* **2015**, *18*, 1213–1225.

(3) Fenno, L.; Yizhar, O.; Deisseroth, K. The Development and Application of Optogenetics. *Annual Review of Neuroscience* **2011**, *34*, 389–412, PMID: 21692661.

(4) Häusser, M. Optogenetics: The age of light. *Nature Methods* **2014**, *11*, 1012–1014.

(5) Cho, Y. K.; Zheng, G.; Augustine, G. J.; Hochbaum, D.; Cohen, A.; Knöpfel, T.; Pisanello, F.; Pavone, F. S.; Vellekoop, I. M.; Booth, M. J.; Hu, S.; Zhu, J.; Chen, Z.; Hoshi, Y. Roadmap on neurophotonics. *Journal of Optics* **2016**, *18*, 093007.

(6) Warden, M. R.; Cardin, J. A.; Deisseroth, K. Optical neural interfaces. *Annual Review of Biomedical Engineering* **2014**, *16*, 103–129.

(7) Pisanello, M.; Pisano, F.; Hyun, M.; Maglie, E.; Balena, A.; De Vittorio, M.; Sabatini, B. L.; Pisanello, F. The Three-Dimensional Signal Collection Field for Fiber Photometry in Brain Tissue. *Frontiers in Neuroscience* **2019**, *13*, 82.

(8) Stujenske, J. M.; Spellman, T.; Gordon, J. A. Modeling the Spatiotemporal Dynamics of Light and Heat Propagation for In Vivo Optogenetics. *Cell Reports* **2015**, *12*, 525–534.

(9) Yizhar, O.; Fenno, L.; Davidson, T.; Mogri, M.; Deisseroth, K. Optogenetics in Neural Systems. *Neuron* **2011**, *71*, 9 – 34.

(10) Pisanello, F.; Sileo, L.; Oldenburg, I. A.; Pisanello, M.; Martiradonna, L.; Assad, J. A.; Sabatini, B. L.; De Vittorio, M. Multipoint-emitting optical fibers for spatially addressable in vivo optogenetics. *Neuron* **2014**, *82*, 1245–1254.

(11) Pisanello, F.; Mandelbaum, G.; Pisanello, M.; Oldenburg, I. A.; Sileo, L.; Markowitz, J. E.; Peterson, R. E.; Della Patria, A.; Haynes, T. M.; Emara, M. S.; Spagnolo, B.; Datta, S. R.; De Vittorio, M.; Sabatini, B. L. Dynamic illumination of spatially restricted or large brain volumes via a single tapered optical fiber. *Nature Neuroscience* **2017**, *20*, 1180–1188.

(12) Pisanello, M.; Patria, A. D.; Sileo, L.; Sabatini, B. L.; Vittorio, M. D.; Pisanello, F. Modal demultiplexing properties of tapered and nanostructured optical fibers for in vivo optogenetic control of neural activity. *Biomed. Opt. Express* **2015**, *6*, 4014–4026.

(13) Pisanello, M.; Pisano, F.; Sileo, L.; Maglie, E.; Bellistri, E.; Spagnolo, B.; Mandelbaum, G.; Sabatini, B. L.; De Vittorio, M.; Pisanello, F. Tailoring light delivery for optogenetics by modal demultiplexing in tapered optical fibers. *Scientific Reports* **2018**, *8*, 4467.

(14) Pisano, F.; Pisanello, M.; Lee, S. J.; Lee, J.; Magie, E.; Balena, A.; Sileo, L.; Spagnolo, B.; Bianco, M.; Hyun, M.; Vittorio, M. D.; Sabatini, B. L.; Pisanello, F. *Nature Methods* **2019**, *16*, 1185–1192.

(15) Čižmár, T.; Dholakia, K. Shaping the light transmission through a multimode optical fibre: complex transformation analysis and applications in biophotonics. *Optics Express* **2011**, *19*, 18871.

(16) Turtaev, S.; Leite, I. T.; Altwegg-Boussac, T.; Pakan, J. M.; Rochefort, N. L.; Čižmár, T. High-fidelity multimode fibre-based endoscopy for deep brain in vivo imaging. **2018**, *7*, 2047–7538.

(17) Tuniz, A.; Schmidt, M. A. Interfacing optical fibers with plasmonic nanoconcentrators. *Nanophotonics* **2018**, *7*, 1279—-1298.

(18) Wang, N.; Zeisberger, M.; Hübner, U.; Schmidt, M. A. Boosting Light Collection Efficiency of Optical Fibers Using Metallic Nanostructures. *ACS Photonics* **2019**, *6*, 691–698.

(19) Liu, M.; Lu, F.; Zhang, W.; Huang, L.; Liang, S.; Mao, D.; Gao, F. Highly efficient plasmonic nanofocusing on a metallized fiber tip with internal illumination of the radial vector mode using an acousto-optic coupling approach. *Nanophotonics* **2019**, *8*, 921—-929.

(20) Minn, K.; Lee, H. W. H.; Zhang, Z. Enhanced subwavelength coupling and nanofocusing with optical fiber-plasmonic hybrid probe. *Opt. Express* **2019**, *27*, 38098–38108.

(21) Li, S.; Yang, S. Nanofocusing of a novel plasmonic fiber tip coupling with nanograting resonance. *Journal of Physics D: Applied Physics* **2020**, *53*, 215102.

(22) Morozov, Y. M.; Lapchuk, A. S.; Prygun, A. V.; Kryuchyn, A. A.; Dostalek, J. Investigation of optical fiber-tip probes for common and ultrafast SERS. *New Journal of Physics* **2020**, *22*, 033027.

(23) Fan, W.; Yan, B.; Wang, Z.; Wu, L. Three-dimensional all-dielectric metamaterial solid immersion lens for subwavelength imaging at visible frequencies. *Science Advances* **2016**, *2*.

(24) Fang, N.; Lee, H.; Sun, C.; Zhang, X. Diffraction-Limited Optical Imaging with a Silver Superlens. *Science* **2005**, *308*, 534–537.

(25) Saleh, B. E. A.; Teich, M. C. *Fundamentals of Photonics*; Wiley, 2007.

(26) Snyder, A. W.; Love, J. D. *Optical waveguide theory*; Chapman and Hall, 1983.

(27) Yizhar, O.; Fenno, L. E.; Davidson, T. J.; Mogri, M.; Deisseroth, K. Optogenetics in Neural Systems. *Neuron* **2011**, *71*, 9–34.

(28) Ciracì, C.; Smith, D. R.; Urzhumov, Y. A. Far-field analysis of axially symmetric three-dimensional directional cloaks. *Opt. Express* **2013**, *21*, 9397–9406.

(29) Ciracì, C.; Urzhumov, Y. A.; Smith, D. R. Effects of classical nonlocality on the optical response of three-dimensional plasmonic nanodimers. *J. Opt. Soc. Am. B* **2013**, *30*, 2731–2736.

(30) Messmer, P.; Bruhwiler, D. L. Simulating laser pulse propagation and low-frequency wave emission in capillary plasma channel systems with a ponderomotive guiding center model. *Phys. Rev. ST Accel. Beams* **2006**, *9*, 031302.

(31) Cowan, B. M.; Bruhwiler, D. L.; Cormier-Michel, E.; Esarey, E.; Geddes, C. G.; Messmer, P.; Paul, K. M. Characteristics of an envelope model for laser–plasma accelerator simulation. *Journal of Computational Physics* **2011**, *230*, 61 – 86.

(32) Terzani, D.; Londrillo, P. A fast and accurate numerical implementation of the envelope model for laser–plasma dynamics. *Computer Physics Communications* **2019**, *242*, 49 – 59.

(33) Roey, J. V.; van der Donk, J.; Lagasse, P. E. Beam-propagation method: analysis and assessment. *J. Opt. Soc. Am.* **1981**, *71*, 803–810.

(34) Wang, P.; Zhao, H.; Wang, X.; Farrell, G.; Brambilla, G. A review of multimode interference in tapered optical fibers and related applications. *Sensors* **2018**, *18*, 858.

(35) Levy, M. *Parabolic Equation Methods for Electromagnetic Wave Propagation*; Electromagnetic Waves; Institution of Engineering and Technology, 2000.

(36) Gloge, D. Optical Power Flow in Multimode Fibers. *Bell System Technical Journal* **1972**, *51*, 1767–1783.

(37) Kutz, J. N.; Cox, J. A.; Smith, D. Mode mixing and power diffusion in multimode optical fibers. *Journal of Lightwave Technology* **1998**, *16*, 1195–1202.